

A redshift-independent theoretical halo mass function validated with Uchuu simulations

Elena Fernández-García¹, Juan E. Betancort-Rijo^{2,3}, Francisco Prada^{1,2}, Tomoaki Ishiyama⁴, Anatoly Klypin⁵, and José Ruedas¹

¹ Instituto de Astrofísica de Andalucía (CSIC), E18008 Granada, Spain,

² Instituto de Astrofísica de Canarias, C/ Via Lactea s/n, Tenerife E38200, Spain

³ Facultad de Física, Universidad de La Laguna, Astrofísico Francisco Sanchez, s/n, La Laguna, Tenerife E38200, Spain

⁴ Digital Transformation Enhancement Council, Chiba University, 1-33, Yayoi-cho, Inage-ku, Chiba, 263-8522, Japan

⁵ Department of Astronomy, University of Virginia, Charlottesville, VA 22904, USA

Received ..., ...; accepted ..., ...

ABSTRACT

We present a new theoretical framework for the halo mass function (HMF) that accurately predicts the abundance of dark matter halos over an exceptionally wide range of masses and redshifts, based on a generalised Press–Schechter model with triaxial collapse (GPS+). The HMF is formulated mainly as a function of the variance of the linear density field, with a weak explicit mass dependence and no explicit redshift dependence, which is able to naturally reproduce the correct normalisation and high-mass behaviour without requiring an empirical fitting. Using the UCHUU N -body simulation suite under *Planck* cosmology, combining six simulations with up to 300 realisations, we measured the HMF over $6.5 \leq \log(M_{200m}/[h^{-1}M_{\odot}]) \leq 16$ and $0 \leq z \leq 20$ with reduced cosmic variance. Over this full domain, we find that GPS+ matches the simulations to within 10–20%, performing similarly to the Sheth–Tormen model at $z \lesssim 2$, but with substantially results at higher redshifts. In the latter case, the Sheth–Tormen model can deviate by 70–80%, while GPS+ will remain within $\sim 20\%$. Finally, we show that the halo mass definition is key: M_{200m} yields a nearly universal, weakly redshift-dependent HMF, whereas adopting the evolving virial overdensity from Bryan & Norman (1998) ends up degrading the agreement at low redshifts and high masses.

Key words. cosmology, dark matter, halos, theory, large-scale structure

1. Introduction

The use of the halo mass function (HMF) to describe the abundance of dark matter halos as a function of mass is a cornerstone of modern cosmology. It encodes the growth of structure from the early Universe to the present day. It provides a fundamental link between theory, simulations, and observations, making it a key probe of cosmological models and parameters (Cooray & Sheth 2002; Mo et al. 2010; Castro et al. 2016). Accurate predictions of its mass and redshift dependence are therefore essential for interpreting data from current and upcoming large-scale structure surveys.

The theoretical foundation of the HMF was laid by the Press–Schechter (PS) formalism (Press & Schechter 1974), later developed through excursion-set theory (Bond et al. 1991; Lacey & Cole 1993) and refined with ellipsoidal-collapse models (Sheth & Tormen 1999; Sheth et al. 2001, hereafter ST). Empirical calibrations based on N -body simulations have since improved its accuracy over a range of cosmologies, halo masses, and redshifts (e.g. Jenkins et al. 2001; Tinker et al. 2008; Despali et al. 2016; Shirasaki et al. 2021; Seppi et al. 2021). However, all existing fits remain limited in scope: early models can be applied mainly to cluster-scale halos at $z \lesssim 3$, while later extensions reach $z \lesssim 10$, but typically only for halo masses above $10^{10} h^{-1} M_{\odot}$. As a result, no current model provides a self-

consistent description of the HMF across the full halo mass hierarchy and cosmic history.

Recent advances in numerical simulations, particularly the UCHUU N -body simulation suite (Ishiyama et al. 2021; Ishiyama et al., in prep.), make it possible to overcome many of these limitations by combining extremely large cosmological volumes with a high mass resolution. This enables precise measurements of the HMF over a vastly extended range of halo masses and redshifts, offering a unique opportunity to revisit and improve theoretical models.

In this work, we build on the generalised Press-Schechter formalism of Betancort-Rijo & Montero-Dorta (2006b,a) and present a new model, named GPS+, which delivers a consistent description of the HMF from dwarf-scale halos to the most massive clusters, spanning $6.5 < \log(M/M_{\odot}) < 16$ and redshifts $0 \leq z \leq 20$. While it remains rooted in the generalised PS framework, triaxial collapse plays a central role in the construction of the model. With minimal calibration to the UCHUU simulations, the resulting HMF depends primarily on the variance of the linear density field, $\sigma(M, z)$, exhibiting only weak explicit mass dependence and with no explicit dependence on redshift. This unprecedented dynamical range and per cent-level accuracy are enabled by the scope and quality of the UCHUU suite, providing a robust framework for interpreting data from ongoing and future surveys such as DESI, Euclid, Subaru PFS, LSST, eROSITA, and JWST.

While our approach is still closely connected to the classical PS picture, it replaces the original collapse assignment with

* e-mail: efdez@iaa.es

a more physically motivated prescription, while preserving the statistical properties of Gaussian random fields and the conceptual structure of Press-Schechter theory.

This paper is organised as follows. Section 2 describes the UCHUU simulations and HMF measurements. The GPS+ theoretical framework is presented in Section 3. In Section 4, we compare the model predictions with simulation results and Section 5 summarises our conclusions.

2. Uchuu simulations

In this work, we tested the theoretical framework using the UCHUU simulation suite spanning a wide range of mass resolutions, including PHI-4096, SHIN-UCHUU, UCHUU, MUCHO-UCHUU-140M, MUCHO-UCHUU-1G, and MUCHO-UCHUU-6G*, as described in Ishiyama et al. 2021; Ishiyama et al., in prep. Their main properties are summarised in Table A.1. The first three simulations are based on *Planck15* cosmology, while the remaining three follow *Planck18*. Despite these slight cosmological differences, their impact on the HMF is negligible compared to both the intrinsic statistical uncertainties of the simulations and the theoretical modelling uncertainties.

We used 50, 300, and 100 independent realisations of MUCHO-UCHUU-140M, MUCHO-UCHUU-1G, and MUCHO-UCHUU-6G, respectively. The HMF is obtained by averaging over all realisations, with uncertainties estimated from the diagonal of the covariance matrix, an ensemble approach that significantly reduces cosmic variance. For the purposes of illustration, within the total volume of $21,600 h^{-3} \text{Gpc}^3$ covered by the 100 MUCHO-UCHUU-6G realisations, the most massive halo is characterised by $M = 8.3 \times 10^{15} M_\odot$, about 13 times the mass of the Virgo cluster (Kashibadze et al. 2020).

All simulations were run with the *TreePM* code *GreeM* (Ishiyama et al. 2009; Ishiyama et al. 2012). PHI-4096, SHIN-UCHUU, and UCHUU were executed on the ATERUI II supercomputer at CfCA, National Astronomical Observatory of Japan, while the MUCHO-UCHUU simulations used the FUGAKU supercomputer at RIKEN, Kobe. Halos were identified with the *RockStar* halo/subhalo finder (Behroozi et al. 2013a) and its distributed version *MPI-Rockstar*[‡] (Tokuue et al. 2024), and merger trees were constructed using *Consistent Trees* (Behroozi et al. 2013b).

Figure 1 shows the combined HMF derived from all the simulations used in this work. We express it in terms of the multiplicity function (e.g Sheth & Tormen 1999), defined as

$$f(M, z) = \frac{M_{200m}}{\rho_m} \frac{dn}{d \ln M_{200m}} \left| \frac{d \ln M_{200m}}{d \ln \sigma} \right|. \quad (1)$$

We adopted the halo mass M_{200m} , defined within an overdensity of $200\rho_b$, where ρ_b is the mean background density. Unlike the virial mass, this fixed-threshold definition is redshift-independent. We refer to Appendix E for more details.

To construct the combined HMF at each redshift, we used halos with at least 407 particles to ensure low-mass completeness. The high-mass end of each simulation is limited to allow for a smooth, continuous transition across overlapping mass ranges. The resulting HMFs are available at the CDS (see Appendix B).

*All simulations are publicly available at <https://skiesanduniverses.org/Simulations/Uchuu/>

[‡]<https://github.com/Tomoaki-Ishiyama/mpi-rockstar/>

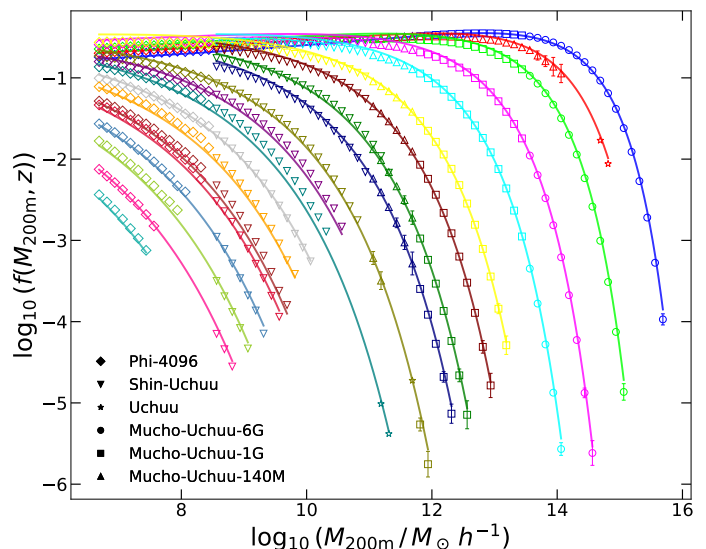


Fig. 1: Multiplicity function $f(M, z)$ (Eq. 1) from UCHUU simulations (markers) vs GPS+ predictions (solid lines) at $z = 0-20$ (right to left; see Table B.2). The y-axis shows the normalised differential halo abundance including $d \ln M / d \ln \sigma$. Only bins with > 200 halos are shown.

3. Theoretical framework

We modelled the HMF using the GPS+ framework, which describes halo abundances over an exceptionally wide mass range ($6.5 \leq \log[M/(h^{-1} M_\odot)] \leq 16$) and up to very high redshifts ($z \sim 20$). The formalism builds on the PS idea that a mass element belongs to a halo of mass larger than M if the smoothed density field satisfies a collapse condition; however, it replaces the original centre-based criterion with a more physically motivated prescription. The model preserves the Gaussian-field statistics underlying PS and excursion-set theory while incorporating the physics of triaxial collapse. In this way, GPS+ retains the conceptual structure of PS but modifies the criterion for assigning mass elements to collapsed objects of mass larger than M .

In this framework, the HMF is given by (Montero-Dorta & Betancort-Rijo 2006):

$$\frac{dn(M, z)}{dM} = \frac{\rho_m}{M} \frac{dF(M, z)}{dM}, \quad (2)$$

where ρ_m is the matter density, and $F(M, z)$ is the mass fraction. The mass fraction is defined as

$$F(M) = \frac{\text{erfc} \left[\langle \delta_c(\sigma(M, z), M) \rangle / (\sqrt{2} \sigma(M, z)) \right]}{V(\Sigma(M, z), M)}, \quad (3)$$

with $V(\Sigma(M, z), M)$ given by

$$V(\Sigma(M, z), M) = 3 \int_0^1 \text{erfc} \left[\frac{\langle \delta_c \rangle(\sigma(M, z), M)}{\sqrt{2} \Sigma(M, z)} \right] \times \sqrt{\frac{1 - \exp(-c(M) \xi^2)}{1 + \exp(-c(M) \xi^2)}} \xi^2 d\xi, \quad (4)$$

where δ_l encodes the linear growth corrections at $z = 0$, $\Sigma(M, z)$ is given by

$$\Sigma(M, z) = \sqrt{\sigma^2(M, z) + U^2(\sigma/\delta_c)}, \quad (5)$$

where $\sigma(M, z)$ is the standard linear-theory variance, and the correction function $U(x)$ is defined as

$$U(x) = -0.01507 + 0.17810 \cdot x + 0.03835 \cdot x^2 - 0.00221 \cdot x^3, \quad (6)$$

where $x = \sigma(M, z)/\delta_c$, and δ_c is the critical overdensity, equal to the linear-theory density contrast, δ_l , in the spherical-collapse approximation at collapse. In our model, the critical overdensity for collapse is further modified as a function of mass and redshift, expressed as

$$\langle \delta_c \rangle = \delta_c \left(1 + 0.845 x - 0.04 x^2 + 0.0025 x^3 \right)^B \times A \left(1 + 0.17 b(M) - 0.087 b^2(M) \right)^D \quad (7)$$

where $b(M)$ is defined by

$$\log b(x) = -1.28 + 0.05781 x - 0.005622 x^2 + 5.884 \times 10^{-4} x^3 - 1.365 \times 10^{-5} x^4, \quad (8)$$

where $x = \log(M/[M_\odot/h])$, while A and B are free parameters fitted to the simulation data (see values below) and D is a parameter whose theoretical value is 1 (see Betancort-Rijo et al., in prep.). However, we did allow it to test the robustness of this prediction. Equation 7 essentially comes from the physics of the triaxial collapse (see Appendix C for the details).

The function $c(M)$ from Equation 4 is a polynomial defined as

$$\log c(x) = -1.124 + 0.01756 \cdot x + 0.002539 \cdot x^2 - 6.438 \times 10^{-5} \cdot x^3 + 4.726 \times 10^{-6} \cdot x^4, \quad (9)$$

where $x = \log(M/[M_\odot/h])$. The quantities entering Eqs. 6–7 follow from the physics of triaxial collapse: U^2 can be obtained from first-principles calculations in Montero-Dorta & Betancort-Rijo (2006) and Eq. 6 is a fit to those results. The functions $b(M)$ and $c(M)$ are fully determined by the linear matter power spectrum (Sánchez-Conde et al. 2007; Betancort-Rijo & Montero-Dorta 2006a). The polynomials given by Eqs. 8 and 9 correspond to fits done in this work for the Planck power spectrum.

This formulation enables the computation of the HMF across a broad halo mass range and out to very high redshifts. A concise overview of the theoretical framework is provided in Appendix C, while a full derivation of the equations will be presented in Betancort-Rijo et al. in prep.

The coefficients A and B in Eq. 7 were obtained by fitting Eq. 2 to the simulation data using the statistic,

$$\chi^2 = \sum_{i,j} \frac{|n_{\text{sim}}(M_i, z_j) - n_{\text{th}}(M_i, z_j)|}{n_{\text{sim}}(M_i, z_j)^2} \left[1 - \Theta \left(\frac{\Delta n_{\text{sim}}(M_i, z_j)}{0.05 n_{\text{sim}}(M_i, z_j)} - 1 \right) \right], \quad (10)$$

where n_{sim} and n_{th} are the simulated and theoretical HMFs, and Δn_{sim} is the statistical uncertainty. The Heaviside function Θ restricts the fit to bins with relative uncertainties below 5%.

Uncertainties were assumed to be Poissonian for simulations with a single realisation (PHI-4096, SHIN-UCHUU, UCHUU), while for MUCHO-UCHUU-140M, MUCHO-UCHUU-1G, and MUCHO-UCHUU-6G, they were derived from the diagonal of the covariance matrix over multiple realisations.

This fit gives $A = 1.089$ and $B = 0.652$. Varying D indicates the best agreement at $D \simeq 1$, consistent with theory. We note that

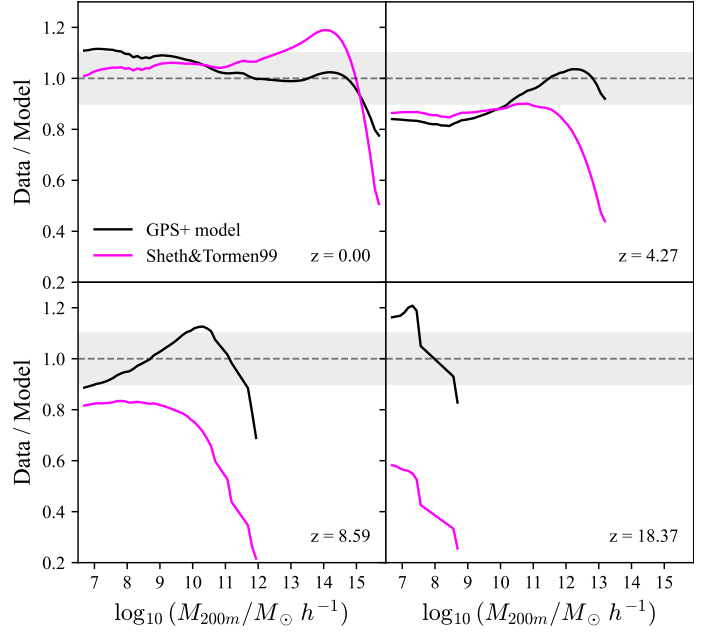


Fig. 2: Ratios of the HMF predictions from GPS+ and ST at different redshifts. Only mass bins with > 100 halos are shown.

only A and B were fitted to the simulations and their values are close to the expected theoretical value of 1.

A key feature of this formalism is that $f(\sigma)$ depends explicitly on mass through the functions $b(m)$ and $c(m)$ (Eqs. 8 and 9), with no explicit dependence on redshift. If this mass dependence is (incorrectly) neglected and we assume that f depends only on σ , we then obtain $f(m, z) = f(\sigma(m, z), m) = f(\sigma, m(\sigma, z)) = f(\sigma, z)$. The first equality is correct: at fixed mass, any redshift dependence enters only through $\sigma(m, z)$. The second equality instead removes the explicit mass dependence of f at fixed σ (a central aspect of our framework) by using the m – σ relation at fixed redshift, thereby introducing spurious σ and redshift dependences.

In our formalism, f depends explicitly on both m and σ ; the artificial redshift dependence appears only when the mass dependence is forced to act exclusively through σ . This leads to the $\sim 50\%$ variation shown in Fig. D.1, about four times larger than the typical modelling uncertainty of the (slightly simplified) framework used here. Since this behaviour follows directly from the explicit mass dependence predicted by the theory, we interpret the trend in Fig. D.1 as lending strong support to the theoretical basis of our formalism.

4. Performance of the theoretical framework and comparison with the Sheth & Tormen HMF

In this section, we present the HMF predicted by the theoretical framework developed and calibrated in this work, comparing it with the UCHUU simulation results described above; for reference, we also include the widely used Sheth–Tormen (ST) model[†], while further comparisons will be presented in Ishiyama et al. (in prep.). Figure 2 shows the ratio between the simulated HMF and the GPS+ prediction across a broad redshift range. At $z = 0$, the ratio remains close to unity over most of the mass range, with deviations reaching $\sim 20\%$ only at the high-mass end

[†]A comparison with the Dark emulator can be seen in Appendix F.

($\log_{10}(M_{200m}/[h^{-1}M_{\odot}]) > 14$), while at $z = 4.27$ similar deviations appear at the low-mass end ($\log_{10}(M_{200m}/[h^{-1}M_{\odot}]) < 11$). At higher redshifts, the agreement improves further, with deviations typically below 10% across nearly the full mass range, demonstrating the robustness and predictive power of the GPS+ model over an exceptionally wide range in mass and redshift.

The ST model, which extends PS by incorporating ellipsoidal collapse and introduces an explicit redshift dependence through the linear growth factor (noting that ST adopts a friends-of-friends mass definition, whereas we use M_{200m}), performs similarly to GPS+ at $z = 0$. At higher redshifts ($z \gtrsim 4.27$), however, GPS+ provides a markedly improved description, particularly for the most massive halos. This discrepancy increases toward earlier times: at $z \approx 18.37$, ST deviates by ~ 60 – 80% , while GPS+ remains within ~ 10 – 20% . These results highlight both the accuracy of our framework across the full mass and redshift domains explored, along with the limitations of existing models when they are extrapolated to the high-redshift regime.

5. Summary

In this work, we present a physically motivated theoretical model for the halo mass function based on a generalised Press-Schechter framework with triaxial collapse (GPS+), which accurately reproduces the HMF measured in the UCHUU cosmological N -body simulation suite, spanning a wide range of volumes and mass resolutions within the *Planck* cosmology. The model is rooted in the PS formalism, but it includes a modified collapse criterion for assigning mass elements to halos above a given mass, as detailed in the appendices. Unlike many previous approaches, GPS+ introduces no explicit redshift dependence, with evolution entering solely through the variance of the linear density field, $\sigma(M, z)$, enabling predictions up to $z \sim 20$ over a halo mass range $6.5 \lesssim \log(M_h) \lesssim 16$. Across this full mass and redshift domain, the model reproduces the simulated HMF with typical deviations below 10–20%, with the largest discrepancies confined to the high-mass end. Compared to the Sheth–Tormen model, GPS+ shows a similar accuracy at $z = 0.0$. However, it provides a substantially improved description at higher redshifts and for the most massive halos, where at $z = 18.37$ Sheth–Tormen deviates by 70–80%, while GPS+ remains within 20%. The uniqueness of this work lies both in the measurement of the HMF over an exceptionally wide mass and redshift range using the UCHUU simulations, paired with the ability of the GPS+ framework to predict the HMF across this range more reliably than any existing model.

We emphasise that our formalism is fully derived from first principles. Only A and B have been allowed to differ from their theoretical values, reflecting the details of our stabilisation model; thus, it is unsurprising that the best fit yields slightly different values.

6. Data availability

The GPS+ model is publicly available on the UCHUU GitHub[‡] and will be included in COLOSSUS[§] (Diemer 2018). The combined HMF from the UCHUU suite is provided in electronic tables (Appendix B). The MUCHO-UCHUU-140M, 1G, and 6G simulation products will be released on the SKIES & UNIVERSES website.

[‡]https://github.com/uchuuproject/HMF_GPSplus

[§]https://bdiemer.bitbucket.io/colossus/lss_mass_function.html

Table B.1 is only available in electronic form at the CDS via anonymous ftp to cdsarc.u-strasbg.fr (130.79.128.5) or via <http://cdsweb.u-strasbg.fr/cgi-bin/qcat?J/A+A/>.

Acknowledgements. This work was supported by project AST22_00001_27, funded by the European Union – NextGenerationEU, the Spanish Ministry of Science, Innovation and Universities, the Recovery, Transformation and Resilience Plan, the Andalusian Regional Government (Junta de Andalucía), and the Spanish National Research Council (CSIC). EFG acknowledges financial support from the Severo Ochoa programme (CEX2021-001131-S, MCIN/AEI/10.13039/501100011033). EFG and FP are supported by the Spanish MICINN grant PGC2018-101931-B-I00. EFG and FP thank the Instituto de Astrofísica de Andalucía (IAA-CSIC), the Centro de Supercomputación de Galicia (CESGA), and RedIRIS for hosting the Uchuu DR1, DR2, and DR3 data releases on the SKIES & UNIVERSES platform. TI acknowledges support from the IAAR Research Support Program at Chiba University, MEXT/JSPS KAKENHI (JP19KK0344, JP25H00662), the MEXT program “Promoting Researches on the Supercomputer Fugaku” (JPMXP1020230406), and JICFuS. The Uchuu simulations were performed on the Aterui II supercomputer at CfCA (NAOJ) and on the K computer at RIKEN, while the Mucho-Uchuu simulations were carried out on Fugaku at RIKEN (Project IDs: hp240184, hp250149). The Uchuu Data Releases made use of the IAA-CSIC computing facilities in Spain (MICINN EU-FEDER grant EQC2018-004366-P).

References

- Behroozi, P. S., Wechsler, R. H., & Wu, H.-Y. 2013a, *ApJ*, 762, 109
 Behroozi, P. S., Wechsler, R. H., Wu, H.-Y., et al. 2013b, *ApJ*, 763, 18
 Betancort-Rijo, J. & López-Corredoira, M. 2000, *ApJ*, 534, L117
 Betancort-Rijo, J. E. & Montero-Dorta, A. D. 2006a, *ApJ*, 653, L77
 Betancort-Rijo, J. E. & Montero-Dorta, A. D. 2006b, *ApJ*, 650, L95
 Bond, J. R., Cole, S., Efstathiou, G., & Kaiser, N. 1991, *ApJ*, 379, 440
 Bryan, G. L. & Norman, M. L. 1998, *ApJ*, 495, 80
 Castro, T., Marra, V., & Quartin, M. 2016, *MNRAS*, 463, 1666
 Cooray, A. & Sheth, R. 2002, *Phys. Rep.*, 372, 1
 Despali, G., Giocoli, C., Angulo, R. E., et al. 2016, *MNRAS*, 456, 2486
 Diemer, B. 2018, *ApJS*, 239, 35
 Ishiyama, T., Fukushima, T., & Makino, J. 2009, *Publications of the Astronomical Society of Japan*, 61, 1319
 Ishiyama, T., Nitadori, K., & Makino, J. 2012, *arXiv e-prints*, arXiv:1211.4406
 Ishiyama, T., Prada, F., Klypin, A. A., et al. 2021, *MNRAS*, 506, 4210
 Jenkins, A., Frenk, C. S., White, S. D. M., et al. 2001, *MNRAS*, 321, 372
 Kashibadze, O. G., Karachentsev, I. D., & Karachentseva, V. E. 2020, *A&A*, 635, A135
 Lacey, C. & Cole, S. 1993, *MNRAS*, 262, 627
 Mo, H., van den Bosch, F. C., & White, S. 2010, *Galaxy Formation and Evolution*
 Montero-Dorta, A. D. & Betancort-Rijo, J. 2006, university of La Laguna, Tenerife, Spain
 Nishimichi, T., Takada, M., Takahashi, R., et al. 2019, *ApJ*, 884, 29
 Press, W. H. & Schechter, P. 1974, *ApJ*, 187, 425
 Sánchez-Conde, M. A., Betancort-Rijo, J., & Prada, F. 2007, *MNRAS*, 378, 339
 Seppi, R., Comparat, J., Nandra, K., et al. 2021, *A&A*, 652, A155
 Sheth, R. K., Mo, H. J., & Tormen, G. 2001, *MNRAS*, 323, 1
 Sheth, R. K. & Tormen, G. 1999, *MNRAS*, 308, 119
 Shirasaki, M., Ishiyama, T., & Ando, S. 2021, *ApJ*, 922, 89
 Tinker, J., Kravtsov, A. V., Klypin, A., et al. 2008, *ApJ*, 688, 709
 Tokue, T., Ishiyama, T., Osato, K., Tanaka, S., & Behroozi, P. 2024, *arXiv e-prints*, arXiv:2412.18629

Appendix A: Simulation Suite Summary

Table A.1 provides a summary of the cosmological N -body simulations used in this work. The simulation suite spans a wide range of volumes and mass resolutions, allowing us to probe dark matter halo statistics across several decades in mass and redshift while controlling for numerical and cosmological systematics.

The Phi-4096, Shin-Uchuu, and Uchuu simulations form a hierarchical set with increasing box size and decreasing mass resolution, all assuming a Planck15 cosmology. These simulations are particularly well suited for studying halo formation and clustering from galactic to large-scale structure scales within a consistent cosmological framework.

Complementing these runs, the Mucho-Uchuu simulations consist of multiple realizations at fixed volumes, adopting a Planck18 cosmology. The Mucho-Uchuu-140M, Mucho-Uchuu-1G, and Mucho-Uchuu-6G sets are designed to improve statistical precision through ensembles of realizations, enabling robust estimates of cosmic variance and covariance in halo statistics. Their differing box sizes and particle masses provide additional leverage to test resolution effects and volume dependence.

For each simulation, Table A.1 lists the total number of particles, box size, dark matter particle mass, Plummer-equivalent gravitational softening length, number of realizations, adopted cosmological parameters, and relevant references. This diverse simulation suite allows for a comprehensive and systematic comparison between numerical results and theoretical predictions across a broad range of scales.

Appendix B: Halo mass function from simulations

Table B.1 provides an example of the release HMF data, corresponding to redshift $z = 0$. This table, along with 19 additional ones (20 in total, with redshifts listed in Table A.2), is available in electronic form at the CDS. Each table includes the following columns: $M200m$, $f(M)$, $\Delta f(M)$, #halos, Simulation, where $M200m$ is the mass enclosed within overdensity $200\rho_b$; $f(M)$ is the multiplicity function (Equation 1); $\Delta f(m)$ is its associated uncertainty; the number of halos corresponds to the count in each mass bin, #; and the simulation name indicates which simulation contributed the HMF measurement for that bin.

Appendix C: Basic considerations about the theoretical framework

The PS formalism yields a halo mass fraction $F(M)$ that is not correctly normalised ($F(M = 0) = \frac{1}{2}$, instead of one). Furthermore, it predicts a high-mass tail that is too steep. This is rather puzzling because, while in other mass ranges there is ample room for improving the theoretical treatment, in this limit the spherical collapse approximation used in the PS formalism should become asymptotically exact. This is due to a selection effect: only proto-halos undergoing an almost perfectly spherical collapse have any chance of having formed by the time being considered. ST combined ellipsoidal collapse with the PS approach and obtained a substantial improvement in the low-mass regime, but they did not solve either the high-mass problem or the normalisation issue.

In Betancort-Rijo & Montero-Dorta (2006b), it was pointed out that the origin of these two problems lies in the PS assumptions themselves. The criterion used by those authors to decide whether a mass element belongs to an object with mass larger than M was that a sphere with Lagrangian radius $r(M)$, centred on that element, satisfies the condition for spherical collapse (i.e.

the linear fractional mass density fluctuation within the sphere, δ_l , obeys $\geq \delta_c$). This criterion cannot be exact, since not all mass elements can be located at the centres of the objects that contain them.

We adopted a more realistic and less restrictive criterion: a mass element belongs to a halo of mass M if it lies within a distance $r(M)$ of a point that satisfies the collapse condition described above. This formulation allows an analytical treatment, leading to the mass fraction $F(m)$ expression in Equation 3, where $V(\Sigma, m)/2$ represents the ratio between the probability that $\delta_l \geq 1.686$ within a sphere with radius $r(M)$ centered on a randomly selected mass element and the greater probability that such an element belongs to an object with mass larger than M . In that work, we used the spherical collapse approximation, so that $\delta_c > (\sigma, M) = \delta_c$ is constant (taken as either 1.686, or, 1.676). Under this formulation, both the high-mass limit and the normalisation behave correctly.

In Montero-Dorta & Betancort-Rijo (2006), we used the Complete Zel'dovich Approximation (CZA) (Betancort-Rijo & López-Corredoira 2000), which effectively corresponds to ellipsoidal collapse, to compute the mean value of δ_l within the region (generally ellipsoidal) that collapses into an object of mass M . We denoted this mean value by $\langle \delta_l \rangle$, and its variance by U^2 . Both quantities were found to depend on M and z only through $\sigma(M, z)$, to a very good approximation). In the present work, the variance obtained in that study has been fitted using the expression given in Equation 6. For $\langle \delta_l \rangle$, the result obtained in that work was

$$\langle \delta_l \rangle = \delta_c \left[0.814 + 0.688 \left(\frac{\sigma}{\delta_c} \right) - 0.033 \left(\frac{\sigma}{\delta_c} \right)^2 + 0.02 \left(\frac{\sigma}{\delta_c} \right)^3 \right]. \quad (\text{C.1})$$

This expression corresponds to the first factor in Equation 7. The second factor introduces a small explicit dependence on M whose origin and derivation will be presented in Betancort-Rijo et al. in prep..

Equation C.1 was obtained using a model for shell-crossing and stabilisation in which the protohalo, upon collapsing along one direction in comoving coordinates to $\frac{1}{13}$ of its original size, becomes stabilised along that axis while continuing to collapse along the remaining directions. This stabilisation model is physically well motivated but not exact, so we introduced the parameters A and B , which are expected to remain close to unity, to account for its approximations.

It is important to note that in this formalism $F(M)$ depends on mass not only through $\sigma(M, z)$, but also through an explicit dependence on M that reflects the shape of the power spectrum at that scale M . This dependence appears in Equation 7 through $b(M)$ (8) and in $V(M)$ (Equation 4) through $c(M)$ (Equation 9).

It should also be emphasised that there is no explicit dependence on redshift, and that $F(M)$ is correctly normalised without requiring parameters fitting. The only fitted parameters are A and B in $\langle \delta_c \rangle (\sigma, M)$, which, based on theoretical considerations, are expected to remain close to unity. In principle, their values could be determined directly from simulations by analysing the behaviour of this function, since analytically we cannot extend the derivation beyond C.1.

Table A.1: Summary of the simulation properties.

Name	N	L [Mpc/h]	M_p [M_\odot/h]	ε [h^{-1} kpc]	#	Cosmology	Ref.
Phi-4096	4096 ³	16	5.13×10^3	0.06	1	Planck15	Ishiyama et al. (2021)
Shin-Uchuu	6400 ³	140	8.96×10^5	0.4	1	Planck15	Ishiyama et al. (2021)
Uchuu	12800 ³	2000	3.27×10^8	4.27	1	Planck15	Ishiyama et al. (2021)
Mucho-Uchuu-140M	1024 ³	140	2.21×10^8	3.75	50	Planck18	Ishiyama et al., in prep.
Mucho-Uchuu-1G	4096 ³	1000	1.26×10^9	8	300	Planck18	Ishiyama et al., in prep.
Mucho-Uchuu-6G	6144 ³	6000	8.04×10^{10}	16	100	Planck18	Ishiyama et al., in prep.

Notes. Number of dark matter particles used in each simulation, box size (L_{box}), dark matter particle mass (M_{part}), gravitational softening length (ε), number of realisations (#), and adopted cosmological parameters.

Table B.1: HMF at $z = 0.0$ from different cosmological simulations.

M_{200b} [M_\odot/h]	$f(M)$	$\Delta f(M)$	#halos	Simulation
4.9×10^6	1.80×10^{-1}	3.5×10^{-4}	2.6×10^5	Phi-4096
...	"
2.7×10^8	2.23×10^{-1}	2.7×10^{-3}	7.1×10^3	Phi-4096
3.7×10^8	2.21×10^{-1}	1.2×10^{-4}	3.6×10^6	Shin-Uchuu
...	"
8.7×10^{10}	2.93×10^{-1}	1.7×10^{-3}	2.8×10^4	Shin-Uchuu
1.2×10^{11}	2.98×10^{-1}	2.8×10^{-3}	4.8×10^5	MU-140M
...	"
4.9×10^{11}	3.27×10^{-1}	5.4×10^{-3}	1.4×10^5	MU-140M
6.5×10^{11}	3.25×10^{-1}	2.8×10^{-4}	7.6×10^7	MU-1G
...	"
2.7×10^{13}	3.33×10^{-1}	1.5×10^{-3}	2.5×10^6	MU-1G
3.7×10^{13}	3.23×10^{-1}	1.4×10^{-4}	4.0×10^8	MU-6G
...	"
4.9×10^{15}	1.07×10^{-4}	1.7×10^{-5}	1.6×10^3	MU-6G

Notes. Columns list: M_{200m} , the halo mass within overdensity $200\rho_b$; $f(M)$, the mass function; $\Delta f(M)$, its uncertainty; the number of halos in each mass bin; and the name of the simulation contributing that bin. Only the first and last bins for each simulation are shown; ellipses indicate omitted intermediate values. Complete tables for all redshifts used in Fig. 1 are available in electronic form at the CDS.

Table B.2: Available snapshots from each simulation.

z	Phi-4096	Shin-Uchuu	Uchuu	MU-140M	MU-1G	MU-6G
0.00	Y	Y	Y	Y	Y	Y
0.49	Y	Y	Y	Y	-	-
1.03	Y	Y	Y	Y	Y	Y
2.03	Y	Y	Y	Y	Y	Y
2.95	-	Y	Y	Y	Y	Y
4.27	Y	Y	Y	Y	Y	-
5.15	-	Y	Y	Y	Y	-
6.34	-	Y	Y	Y	Y	-
7.03	-	Y	Y	Y	Y	-
8.58	Y	Y	Y	Y	Y	-
9.47	Y	Y	Y	Y	Y	-
10.44	Y	Y	Y	Y	Y	-
11.50	Y	Y	Y	Y	Y	-
12.66	Y	Y	Y	Y	Y	-
13.93	Y	Y	Y	Y	-	-
14.32	Y	Y	-	-	-	-
15.57	Y	Y	-	-	-	-
16.92	Y	Y	-	-	-	-
18.37	Y	Y	-	-	-	-
19.95	Y	Y	-	-	-	-

Notes. 'Y' indicates that a snapshot exists at the corresponding redshift, and '-' indicates that no snapshot is available for that simulation. MU denotes the MUCHO-UCHUU simulations.

Appendix D: Multiplicity function as a function of $\sigma(M)$

In this appendix, we show the multiplicity function, $f(\sigma, z)$, as a function of σ at different redshifts, as predicted by the GPS+ model presented in this work (Figure D.1).

Appendix E: Dependence of the HMF with the halo mass definition

As part of this work, we assessed the impact of different halo mass definitions in our theoretical framework. The HMF results presented in Section 4 are based on the M_{200m} mass definition; however, the virial mass, M_{vir} , can also be adopted. Figure E.1 compares the performance of the model under both definitions. The largest differences arise at low redshift. When using the virial mass, the agreement at the high-mass end worsens significantly, with ratios dropping to ~ 0.5 , corresponding to discrepancies of $\sim 50\%$ between the model predictions and the measured HMFs from the simulations. At higher redshifts, the

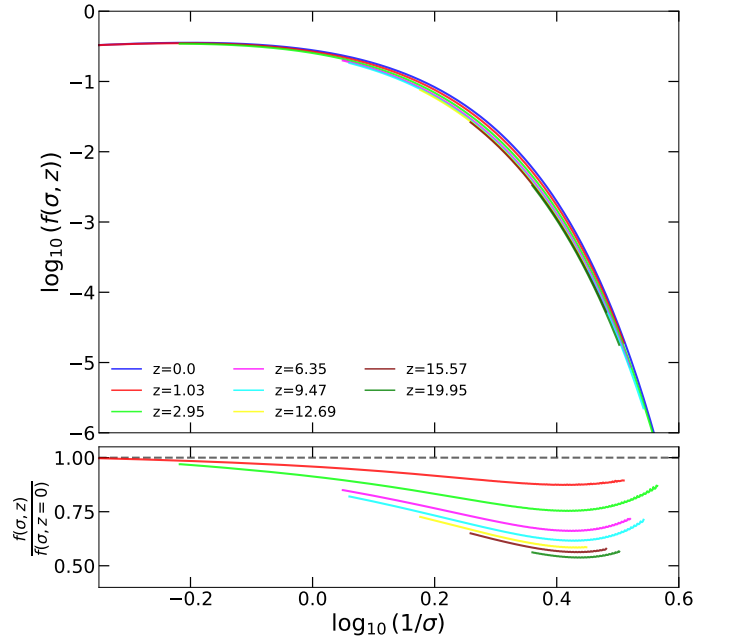


Fig. D.1: Top panel: Multiplicity function $f(\sigma, z)$ as a function of σ at different redshifts, as predicted by the GPS+ model presented in this work. Bottom panel: Ratio of the model at each redshift to $z = 0$ prediction.

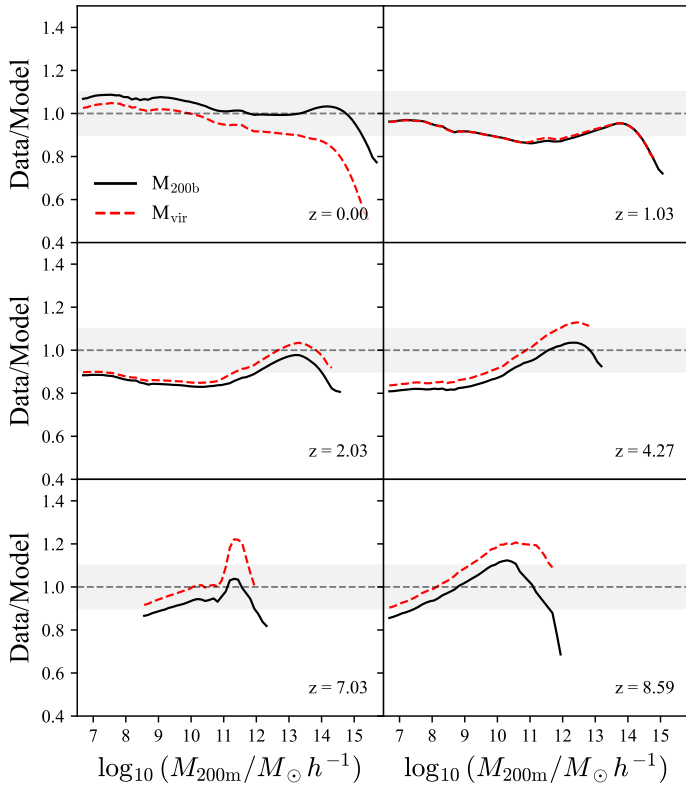


Fig. E.1: Comparison of the ratio between the simulated HMF and the GPS+ model at different redshifts, for two halo mass definitions in the data: the mass enclosed within overdensity $200\rho_b$, M_{200m} , and the mass within the virial radius, M_{vir} .

performance of the model using the virial mass becomes comparable to that obtained using the M_{200m} definition.

This analysis shows that the choice of halo mass definition has a strong impact on the performance of the model, particularly at low redshifts, where the difference between M_{vir} and M_{200m} becomes significant. The virial mass definition does not appear to be suitable in this context, as no choice of fitted parameters yields a good agreement at the high-mass end of the HMF at $z = 0.0$. This behaviour is related to the fact that the virial overdensity, Δ_{vir} , is not constant. In the Uchuu simulation suite, Δ_{vir} evolves following Bryan & Norman (1998), giving $\Delta_{vir}(z = 0) \approx 102$, $\Delta_{vir}(z = 1.03) \approx 159$, and approaching the Einstein–de Sitter value of 178 at higher redshift. That work argues that the density contrast at virialisation should depend on Ω_m (and thus on redshift for Λ CDM cosmologies). However, there are strong counterarguments suggesting that Δ_{vir} should be nearly independent of redshift. A detailed discussion of this point and its theoretical implications will be presented in Betancort-Rijo et al. in prep.; here, we simply highlight that the available evidence points toward a weak or negligible redshift dependence of Δ_{vir} . In Sánchez-Conde et al. (2007), we investigated the spherical collapse model with shell-crossing to study the stabilisation of proto-halos and no difference was found amongst the Einstein–de Sitter and Λ CDM cosmologies.

If the results of Bryan & Norman (1998) were correct and the stabilisation process truly depended on redshift, then the HMF constructed using M_{200m} should exhibit explicit redshift dependence. In that case, the formalism presented here - which contains no explicit dependence on z - would be unable to reproduce the simulation results accurately. Conversely, the HMF constructed using M_{vir} , together with its redshift-dependent Δ_{vir} ,

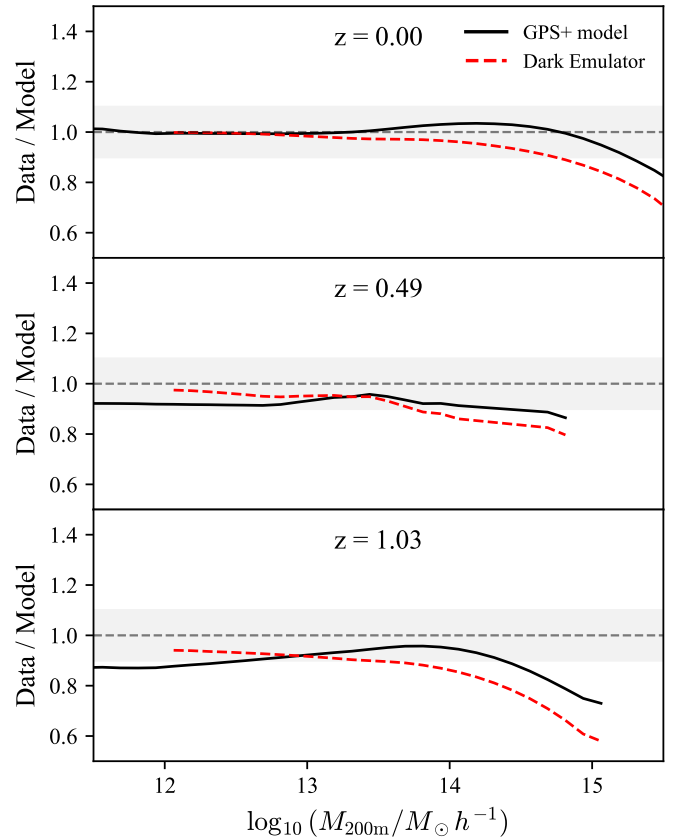


Fig. F.1: Comparison of halo mass function ratios using two different theoretical predictions. Each panel shows the ratio of the data to the GPS+ model prediction and to the Dark Emulator prediction, highlighting relative differences between the two approaches. The panels correspond to redshifts $z = 0.00$ (left), $z = 0.49$ (middle), and $z = 1.03$ (right).

would account for the assumed redshift dependence of the stabilisation process and thus eliminate this source of spurious explicit redshift dependence. Under such circumstances, the HMF based on M_{vir} would be expected to appear more universal.

However, Figure E.1 shows the opposite behavior: the HMF constructed using M_{200m} provides a significantly better match to the formalism (which is explicitly independent of z), and therefore yields a more universal HMF.

It should be noted that in Figure E.1, the M_{vir} data from the simulations are compared with the predictions of the formalism using parameter values slightly adjusted relative to those employed for M_{200m} , in order to obtain the best possible agreement across the full redshift range. Even with this optimisation, the model fails to accurately reproduce the HMF at low redshift when using M_{vir} at $z = 0$, there is a pronounced discrepancy for high-mass end, while for $z = 1.03$ and larger z 's the difference residues for both mass definitions are within the accuracy of the formalism. Since for these redshifts Δ_{vir} changes little according to Bryan & Norman (1998) formalism, this supports the conclusion that Δ_{vir} is in fact almost independent of redshift.

Appendix F: Comparison with the Dark Emulator

We compare the GPS+ model with the predictions from the widely used Dark Emulator (Nishimichi et al. 2019), which is calibrated only up to $z = 1.48$ and for $M_{200m} \gtrsim 10^{12} h^{-1} M_\odot$;

therefore, the comparison is restricted to redshifts below this limit.

Figure F.1 presents the ratios of the data relative to the HMF predicted by the GPS+ model and by the Dark Emulator at $z = 0.0$ (left panel), $z = 0.49$ (middle panel), and $z = 1.03$ (right panel). The Dark Emulator fails to reproduce the U_{CHUU} HMF at low halo masses and systematically overpredicts the HMF at the high-mass end. Overall, the GPS+ model shows significantly better agreement with the simulation data across the full mass range considered.